

Article

Doping Silica Fume Enhances the Mechanical Strength of Slag/Fly Ash Geopolymer Paste under Frost Attack

Sen Wang, Yuqing Liang, Duosi Mo, Chonghui Zhang, Jiwei Xue , Xuewen Song  and Yachao Wang * 

School of Resources Engineering, Xi'an University of Architecture & Technology, Xi'an 710055, China; wangsen@xauat.edu.cn (S.W.); lyq990503@163.com (Y.L.); moduosi@xauat.edu.cn (D.M.); zhangchonghui@xauat.edu.cn (C.Z.); xjw635171816@xauat.edu.cn (J.X.); songxwhl@163.com (X.S.)

* Correspondence: wangyachao@xauat.edu.cn

Abstract: Benign design of alkali-activated slag/FA geopolymer paste has attracted increasing attention for optimizing its service performance. Therefore, the replacement of fly ash (FA) with 10 wt% silica fume (SF) is investigated by mechanical strength after freeze–thawing cycles and microstructure characterization. The results show that an appropriate dosage (30 wt%) of slag is necessary to prepare heat-free curing alkali-activated slag/FA geopolymer paste with excellent mechanical performance. The SF/slag/FA (SF:slag:FA = 10:30:60, wt%) geopolymer paste exerts an enhanced compressive and flexural strength of 95.2 and 3.2 MPa, respectively. Meanwhile, the doped 10 wt% SF facilitates the propagation of (N, C)-A-S-H chains, rather than the formation of C-S-H gels. It is evidenced by the absent exothermic peak at about 861 °C from the differential scanning calorimetry (DSC) curves. The pores volume and tortuosity also rise for the pore diameter < 20 nm from mercury intrusion porosimeter (MIP) results, corresponding to an improved freezing–thawing resistance with the residual compressive strength of 52.8 MPa and the weight loss of 10.5% after 300 freeze–thawing cycles. It explores a cost-effective and benign facile approach to designing heat-free curing alkali-activated slag/FA geopolymer paste with good freezing–thawing resistance.

Keywords: alkali-activated; freezing–thawing; fly ash; geopolymer; silica fume



Citation: Wang, S.; Liang, Y.; Mo, D.; Zhang, C.; Xue, J.; Song, X.; Wang, Y. Doping Silica Fume Enhances the Mechanical Strength of Slag/Fly Ash Geopolymer Paste under Frost Attack. *Minerals* **2023**, *13*, 925. <https://doi.org/10.3390/min13070925>

Academic Editors: Brajendra Mishra, Manish Kumar Sinha and Himanshu Tanvar

Received: 6 June 2023
Revised: 27 June 2023
Accepted: 6 July 2023
Published: 10 July 2023



Copyright: © 2023 by the authors. Licensee MDPI, Basel, Switzerland. This article is an open access article distributed under the terms and conditions of the Creative Commons Attribution (CC BY) license (<https://creativecommons.org/licenses/by/4.0/>).

1. Introduction

Geopolymers are currently being developed as an environmentally beneficial alternative to Portland cement for concrete production, offering comparable performance and cost-efficient techniques while reducing greenhouse gas emissions [1,2]. Geopolymerization could convert a wide range of metallurgical waste aluminosilicate materials including fly ash (FA), slag, and steel slag into cementitious materials, such as pastes and binders. Nevertheless, the multifunctional design of geopolymers has attracted increasing attention by adjusting multi-component metallurgical solid wastes [3–5], such as fire protection, thermal stability, and ultra-high toughness, as well as the freezing–thawing resistance.

Meanwhile, previous reports have manifested that slag affects most of the physical and chemical properties of the alkali-activated slag/FA paste, playing an important role during synthesis and also in determining long-term durability [6,7]. It has been determined that noticeable amounts of slag exert a strengthening effect on the preparation of FA-based geopolymers cured at room temperature (RT), rather than the heating curing at about 80 °C for energy saving. Ismail et al. [8] investigated the performance of alkali silicate-activated FA/slag geopolymer binders subjected to sulfate exposure. Because the main products of alkali-activated FA/slag contain hydrotalcite and C-S-H gels, they lead to an increase in the total amount of chemical shrinkage [9]. Nevertheless, the mechanical strength of the alkali-activated slag/fly ash geopolymer paste under frost attack remains to be studied to meet the requirements of cold regions.

However, the alkali-activated slag/FA binder possesses strong fragility and poor pliability; a lot of methods have been explored to reinforce and toughen the binder [10,11].

To track this problem with a cost-effective approach, the incorporation of other solid wastes has been attracting increasing attention, such as calcium carbide residue and Glauber's salt [12], calcium carbide slag and sodium metasilicate powder [13], and salt-loss soda residue and oxalate acid [14], as well as the waste perlite powder [15]. Therefore, the multicomponent geopolymer consists of various solid wastes and is in full swing to pursue high-performance and multi-function cementitious materials, such as freezing–thawing resistance and cost effectiveness. Essentially, the alkali activation is the chemical interactions between cations like K^+ , Na^+ , and Ca^{2+} and anions like CO_3^{2-} , OH^- , $Al(OH)^-$, SiO_3^{2-} , and PO_4^{3-} , the depolymerized silica tetrahedra are prone to crosslink the activated aluminum-oxygen tetrahedra or octahedral and transform into N-(C)-A-S-H chains or networks [13–15], and the cations are trapped into the networks for equilibrium charge.

Currently, very few studies have taken silica fume (SF) into account for further optimizing the service property of alkali-activated slag/FA binder. Theoretically, SF possesses an amorphous structure and high reaction activity, which has attracted much attention and investigation in the Portland cement system. However, in the non-sintered cement system, SF-derived activators give reaction products that are very similar to those obtained using commercial silicate solutions. As a consequence of the high reactivity of this precursor, SF provides high concentrations of Si to the systems from the early stages of the reaction [16]. Jose et al. [17] suggest that the optimum silica replacement is 5%–10%, served as heterogeneous nucleation centers for the hydration products after the dissolution of the glassy slag by the alkali-activation.

Thus, the mechanical strength of SF-doped alkali-activated slag/FA binder needs to be further clarified to explore low-cost geopolymers with high performance. Additionally, the frost-thawing resistance of alkali-activated binder is also crucial to evaluate its usability [18], especially for the severe-cold regions. Because of the coupling effect of internal frost-heave stress induced by phase transition and external frost-heave stress induced by ice contraction [19], the alkali-activated slag/FA binder is vulnerable and fragile to undertake the frost attack. Regarding the SF-doped alkali-activated slag/FA binder, the SF could improve the mechanical strength. But the freeze–thaw resistance of the ternary binder needs to be clarified because a higher compressive strength does not necessarily indicate a better freeze–thaw resistance [20].

Consequently, the identification of a strong correlation between FA, slag, and SF in the slag/FA binder studied here is significant in determining whether these materials would meet wide approval in the local market. It is necessary to explore a simple-yet-effective solution for the utilization of industrial solid waste. The primary purpose of this paper is to address the following questions based on the optimum slag dosage in alkali-activated slag/FA-based geopolymer and micro-structure evaluation of SF doped slag/FA binder is investigated through the replacement of FA with 10 wt% SF [21]. The mechanical properties, freeze–thaw resistance, pore structure, differential scanning calorimetry (DSC), morphology, and x-ray diffraction (XRD) spectra are studied systematically to clarify the SF effect on the freeze–thaw resistance of slag/FA geopolymer paste. Generally, it explores a cost-effective, benign facile approach to design heat-free curing alkali-activated slag/FA geopolymer paste with good freezing–thawing resistance. It clarifies the reactive priority between the (N, C)-A-S-H chains and the C-S-H gels to construct durable cementitious materials.

2. Materials and Characterizations

2.1. Starting Materials

FA with a Blaine-specific surface area of $500\text{ m}^2/\text{kg}$ after oven drying at $105\text{ }^\circ\text{C}$ and ball-milling for 1 h was obtained from Hancheng power plant in China. Granulated ground blast furnace slag (slag) was obtained from Delong powder company with a Blaine-specific surface area of $420\text{ m}^2/\text{kg}$. Silica fume (SF) was derived from Linyuan chemical reagent company. The mean particle size of FA, slag, and SF was $11.2\text{ }\mu\text{m}$, $15.5\text{ }\mu\text{m}$, and $6.9\text{ }\mu\text{m}$, respectively, tested by the laser diffraction particle size distribution instrument (Haixinrui company of Beijing in China, HL5500) according to the standard of GB/T19077.1-2019

or ISO 13320-2020. The particle size distribution of the three kinds of powder presents a normal distribution with one symmetrical peak corresponding to the mean particle size approximately. The chemical compositions of raw materials were given in Table 1. Alkali activator, $\text{Na}_2\text{SiO}_3 \cdot 9\text{H}_2\text{O}$ (A.R.), presented spherical grains with an activator modulus of 1.0, was purchased from Tianjin Yaohua chemical reagent company of China.

Table 1. Chemical compositions of raw materials.

Raw Materials	Mass Percent (wt%)									
	CaO	SiO ₂	Al ₂ O ₃	Fe ₂ O ₃	MgO	Na ₂ O	K ₂ O	SO ₃	TiO ₂	Loss
Fly ash	3.82	55.18	31.19	5.07	0.60	0.29	1.99	0.28	1.05	0.53
Slag	37.65	31.29	14.31	0.61	8.51	0.63	0.58	4.94	0.83	0.54
SF	0.60	87.18	6.89	1.18	0.45	0.28	0.66	0.32	-	2.11

2.2. Preparation of Specimens

The heat-free curing alkali-activated slag/FA geopolymeric binder was synthesized by adding sodium silicate (15 wt%, $\text{Na}_2\text{SiO}_3 \cdot 9\text{H}_2\text{O}$) solution into the uniform mixture of FA and slag with a water/(slag + FA) ratio of 0.3 to form the slurry in a cement mortar machine, the weight ratio of FA to slag was 80/20, 70/30, and 60/40, respectively. Then the slurry was poured into a stainless triplet mold of $160 \times 40 \times 40 \text{ mm}^3$, demoulded after curing for one day in a standard curing box of cement at room temperature (RT). Finally, the specimens were put into a curing box for another 27d at RT with an 85% relative humidity. Based on the optimum slag dosage in alkali-activated slag/FA geopolymer, the replacement of FA with 10 wt% SF was studied, and therefore the weight ratio of SF:slag:FA was 10:30:60 as the starting materials to prepare the specimen. Freeze–thaw cycles were performed by ASTM C666, Procedure A, and the test was conducted by Hengnai measurement apparatus with one freeze–thaw cycle conducted in 2–5 h; the thawing time should not be less than a quarter of the total time of one cycle. At the end of freeze–thawing, the temperature of the specimen center should be controlled at $-18 \text{ }^\circ\text{C}$ and $5 \text{ }^\circ\text{C}$, respectively.

2.3. Characterizations

Compressive strengths were tested by a full-automatic cement compressive testing machine of YAW-300 type with a pressurization rate of 2.4 kN/s; the testing error was 0.5 MPa. Flexural strengths were measured by a motorized bending tester of DKZ-5000 type; the testing error was 0.2 MPa. Micro-morphology analysis of samples was conducted on a Quanta 200 scanning electron microscope (SEM) with a working condition of 20 kV voltage. Pore size distributions of samples after 28d curing were tested by an AUTOPORE 9500 mercury intrusion porosimeter (MIP) with a tortuosity measurement of the sample under nitrogen pressure of 0.3 MPa; the testing error of tortuosity was 2. XRD patterns of specimens were conducted on a D/MAX-2400 X-ray diffractometer equipped with a rotation anode using $\text{Cu K}\alpha$ radiation. Differential scanning calorimetry (DSC) of Mettler tested the heat flow of specimens after 28d of curing, it was conducted during the heating process of $50\text{--}950 \text{ }^\circ\text{C}$ under a nitrogen atmosphere at a heating rate of $30 \text{ }^\circ\text{C}/\text{min}$.

3. Results and Discussion

3.1. Mechanical Properties of Specimens

Figure 1 displays the compressive strengths of specimens, which climbs with the increasing dosage of slag. It determines that incorporated slag facilitates a higher cementitious reactivity with a substantial increase in compressive strength. The 28d compressive strength of the specimen with 40 wt% slag reached 82.3 MPa while it was 66.8 MPa for the specimen with 20 wt% slag, which revealed that the active calcium derived from slag plays an important role in improving the mechanical performance. It is proposed [14,22] that the hardening process is initiated by the precipitation of C-S-H/(N, C)-A-S-H gels together and that rapid hardening continues on account of accelerated geopolymerization.

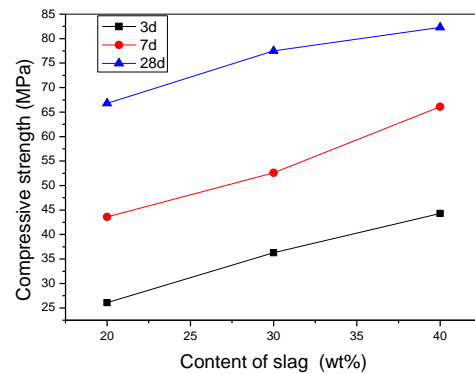


Figure 1. Compressive strength of specimens.

On the contrary, the 28d flexural strength of the specimen with 40 wt% slag decreases sharply after 7d curing as shown in Figure 2. It dropped to 1.8 MPa while it was 2.6 MPa for the specimen with 30 wt% slags, implying that excess free calcium exerts a reverse effect, to the disadvantage of the flexural strength. Due to the interruption of the (N, C)-A-S-H chain gels by the newly formed C-S-H gels, inhibiting or impeding the chain propagation, more interfaces or cracks form and grow, leading to a decrease in flexural strength. As a whole, it determines that there is a critical dosage (30 wt%) of slag content for slag/FA geopolymer paste to attain excellent compressive strength as well as flexural strength.

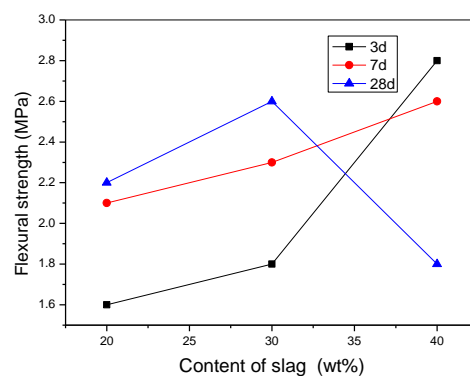


Figure 2. Flexural strength of specimens.

Meanwhile, the mechanical performance of SF doped slag/FA (SF:slag:FA = 10:30:60, wt%) binder is shown in Figures 3 and 4, using the alkali-activated slag/FA (30:70, wt%) binder as the reference. The 28d compressive strength is improved to 95.2 MPa (increased by 22.8%) and the flexural strength rises to 3.2 MPa (increased by 23.1%) after replacement of 10 wt% FA with SF. It demonstrates that incorporating SF into slag/FA binder is an effective method to alleviate the inherent fragility of alkali-activated slag/FA binder. This is because the more amorphous $\text{Si}(\text{OH})_4$ derived from the SF is prone to crosslink with the (N, C)-A-S-H chain, rather than transform into C-S-H gels, as evidenced by the simultaneously increased flexural strength, compared with the reduced flexural strength of sample 40S.

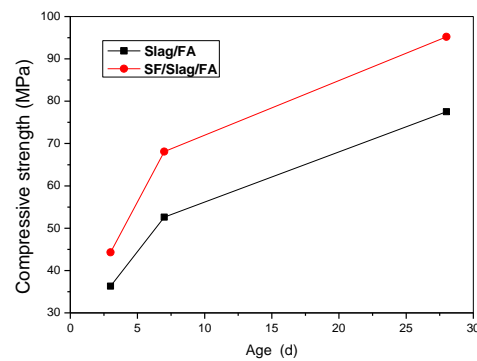


Figure 3. Compressive strength of SF/slag/FA binder.

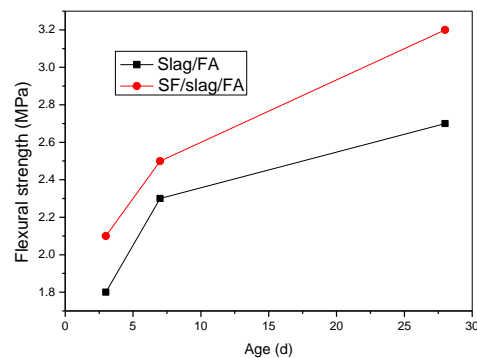


Figure 4. Flexural strength of SF/slag/FA binder.

3.2. Pore Distributions of Specimens

The pore size distributions of specimens are summarized in Table 2. Combined with the mechanical performance, it is found that the median pore diameter and total porosity are inversely proportional to the compressive strength. The median pore diameter of the specimen drops from 48.2 nm to 6.4 nm with the increasing slag dosage gradually. Meanwhile, the pore volume of pore with a diameter < 20 nm increases following the compressive strength because the FA is transformed into geopolymerical gels and slag, which could hydrolyze to active C-H-S and (N, C)-A-S-H sols under an alkaline environment. They could insert and fill into the clearance of the cross-linked network derived from the gels, forming a compact microstructure with a lower porosity and a reduced median pore diameter.

Table 2. Pore size distributions of specimens.

Specimens	<20 nm (%)	20–200 nm (%)	0.2–3 μm (%)	>3 μm (%)	Median Pore Diameter (nm)	Porosity (%)	Tortuosity
20S	0.02	41.18	10.03	48.76	48.2	21.05	12.44
30S	32.25	18.62	7.79	41.34	7.7	19.08	60.37
40S	40.02	9.17	11.39	38.43	6.4	20.93	81.74
30S + 10SF	41.16	3.14	35.81	19.88	5.6	13.47	116.9

Note: 20S—incorporating 20 wt% slags into FA, 30S—incorporating 30 wt% slag into FA, 40S—incorporating 40 wt% slags into FA, 30S + 10SF—incorporating 30 wt% slag and 10 wt% SF into FA.

Interestingly, the increasing tortuosity matches the improvement of compressive strength value, the compact micro-structure holds tortuous pore channels which are triggered by the filling effect of the amorphous paste. Song et al. [23,24] suggest that the increase of tortuosity with hydration is indicative of both the filling of pores and the decreasing connectivity of the pore structure in an alkali-activated slag system because slag pastes have a very disconnected pore structure. Combined with the former reports, it determines that tortuosity could be used as a critical measure of mechanical properties.

Because the coexistence of C-S-H and (N, C)-A-S-H mainly derives from slag and amorphous geopolymer, more disconnected pore and cross-link network structures reconstruct prompting more irregular and tortuous structure of the binder. This is in agreement with the investigation of Collins et al. [25] that the capillary pores within alkali-activated slag concrete have variable cross-section shape, surface roughness, tortuosity, and random meeting and divergence with adjacent pores.

It is the replacement of FA with 10 wt% SF that diminishes the porosity (13.47%) and improves the tortuosity (116.9) as is evident in Table 2. More as-formed $\text{Si}(\text{OH})_4$ hydrolyzed from the incorporation of SF into the alkali-activated slag/FA system boosts and extends the $\equiv\text{Si}-\text{O}-\text{Si}\equiv$ chains due to the polycondensation or cross-linking. It promotes the formation of electronegative polymeric cages with three-dimensional networks and the Ca^{2+} is easily attracted and trapped into the cages for equilibrium charge.

3.3. Mechanical Properties of Specimens Subjected to Freeze–Thaw Cycles

The residual compressive strength and weight loss of specimens subjected to freeze–thawing cycles are shown in Figures 5 and 6. It presents a continuous decline with the increasing cycle, but the residual compressive strength of the SF-containing specimen drops from 95.2 to 52.8 after 300 cycles (decreasing by 44.5%), while that of the specimen without SF decreases by 92.8%. However, the weight loss of the specimen without SF attains 56.4% while that of the SF-containing specimen is only 10.5 wt% after 300 cycles. It demonstrates that ternary SF/slag/FA binders hold higher frost resistance than binary specimens without SF.

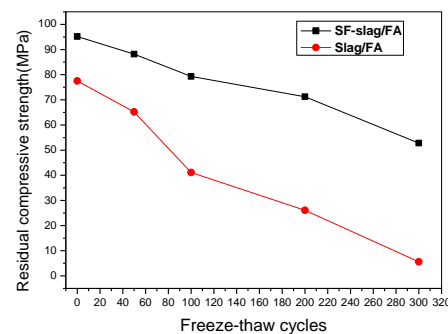


Figure 5. Compressive strengths of binders.

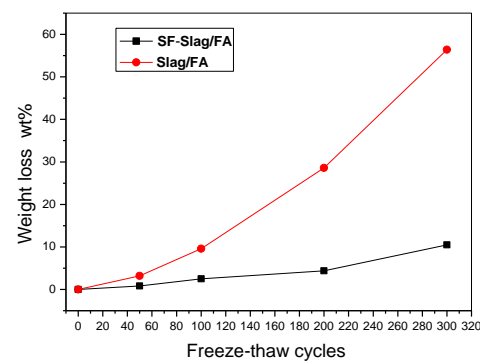


Figure 6. Weight losses of binders.

Combined with the results of pore size distribution, the lower porosity and higher pore volume with a pore diameter < 20 nm after incorporating SF favor a lower absorption of free water. Therefore, the expansion stress derived from the freeze–thawing of water involved in the matrix decreases and suspends the deterioration of specimens because the addition of SF in Portland cement causes a significant slowdown of capillary water uptake and a higher frost resistance [26,27]. Sun et al. [28] also suggest that the freeze–thawing durability of FA-based alkali-activated mortars is superior to that of Portland cement mortars. This

implies that SF holds great potential to improve the frost resistance of inorganic siliceous binders to some extent.

During the freezing–thawing cycles, (i) freezing increases hydraulic water pressure and augments volume; (ii) ice crystals are formed within the capillary pores; and (iii) in the liquid state, the lack of acid–base equilibrium results in osmotic pressure [19,29]. The doped SF could transform into reactive $\text{Si}(\text{OH})_4$ under alkaline activation, which could crosslink the (N, C)-A-S-H and facilitate the chain propagation, leading to an increase in the pore volume with a pore diameter < 20 nm, as well as reduced free water within the paste. Li et al. [30] propose that the effects of nano-nucleation, nano-filling, crack arrest, and mechanical interlocking of modified carbon nanotubes make geopolymer mortars denser, decreasing the percentage of the capillary pore. Chen et al. [31] also assert that the as-formed C–S–H gel further fills the capillary pores and diminishes the frost attack. Generally, the doped SF facilitates the propagation of the (N, C)-A-S-H chains within the ternary SF/slag/FA binder, improving its freezing–thawing resistance effectively.

3.4. XRD Analysis

The XRD spectra are shown in Figure 7, and the coexistence of mullite, quartz, tobermorite, and hydrated calcium silicate is displayed in the samples. Noticeably, there is a hump between $2\theta = 15\text{--}38^\circ$ due to the amorphous silicates involved in the paste specimen. The hump area of the SF-containing specimen is larger than that of the specimen without SF ($A_2 > A_1$), corresponding to the increased content of vitreous silicates to some extent, matching the higher mechanical strength. The amorphous silicates mainly consist of the (N, C)-A-S-H and the C-S-H gels, which derive from the reconstruction of the activated $[\text{Si}(\text{OH})_4]$ and $[\text{Al}(\text{OH})_4]^-$, as well as the active C-H-S from the slag. Enhanced crosslinking or chain propagation is crucial for obtaining excellent mechanical strength and the enhanced silicates indicate that the doped SF favors the crosslinking and reconstruction of amorphous silicate chains.

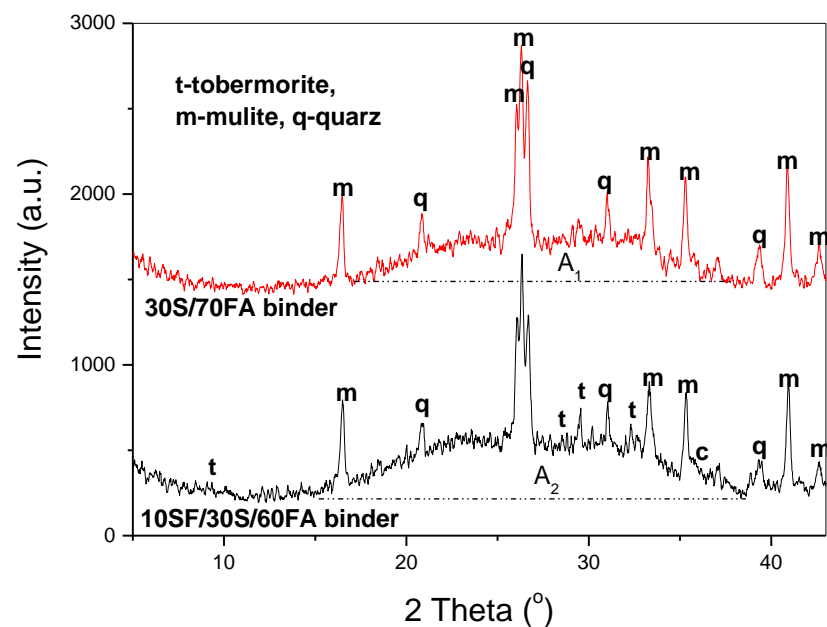


Figure 7. XRD of samples.

Meanwhile, the mullite and quartz belong to inert substances derived from FA, which are inert to participate in the geopolymerization. However, the slightly characteristic peaks of tobermorite are detected after the substitution of 10 wt% SF for 10 wt% FA. It is demonstrated that active silicon dioxide favors the formation of tobermorite to some extent. Combined with this, excessive Ca^{2+} is detrimental to flexural strength whereas the SF-containing geopolymer is beneficial to improve flexural strength. Therefore, the doped

SF also favors the chain propagation of the amorphous silicates of (N, C)-A-S-H. However, the XRD patterns of specimens subjected to freezing–thawing cycles are absent, due to the nearly identical spectra detected for all SF-containing specimens. This is because the freezing–thawing cycles mainly generate the frost-heave stress induced by phase transition and ice contraction, rather than the mineral-phase transformation, thus identical spectra do not appear.

3.5. DSC

The heat flow curves of the samples are shown in Figure 8, illustrating that continuous heat absorption occurs on the samples. There is a clear endothermic peak during 50–200 °C predominantly, which is assigned to the free water evaporation involved in the microvoids and dehydration of the calcium-rich silicate gels. The specimen of 40 s possesses an increased endothermic peak of 145 °C, compared with the 105 °C for the specimen of 20 s approximately. It shifts slightly to a higher temperature with the increasing content of slag, due to the increased content of C-S-H because the new-formed C-S-H holds cementitious reactivity to fill and insert the pores of geopolymer paste, leading to a decrease in the pore diameter. Combined with the results of MIP, it deduces that the smaller median pore diameter facilitates the higher evaporation temperature. Zhang et al. [10] suggest that the resin has a filling effect and improves the evaporation temperature in alkali-activated metakaolin/slag-based geopolymer.

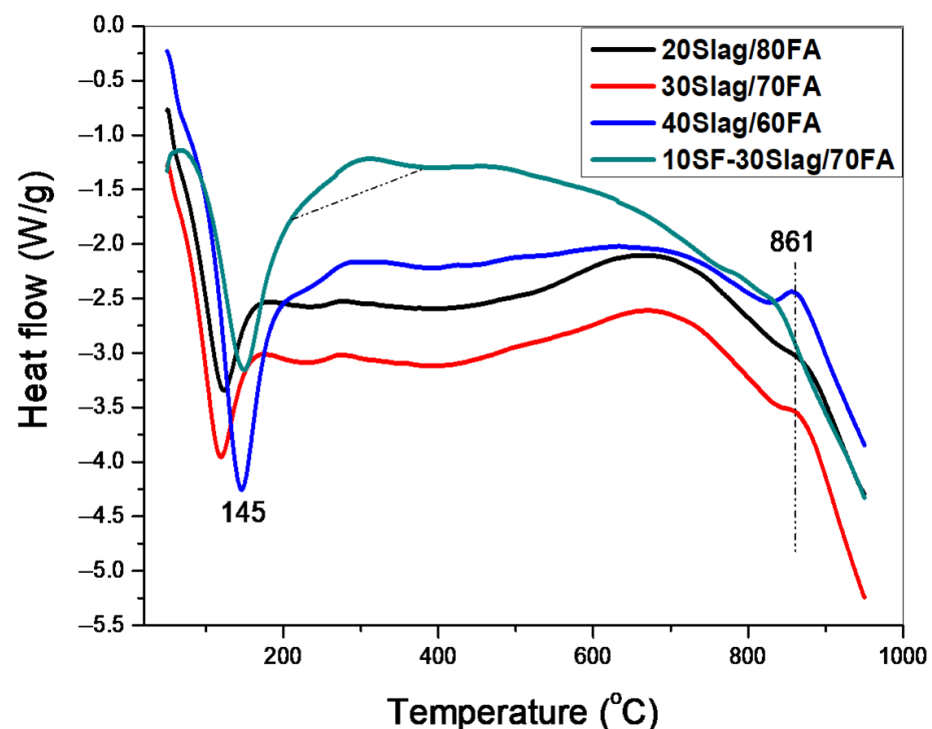


Figure 8. Heat flow curves of samples.

Meanwhile, there is no endothermic peak during 300–500 °C, indicating that the calcium hydroxide does not exist in the sample. On the other hand, the area of the endothermic peak increases and a slight exothermic peak appears with the increase of slag amount. The alkali-activated slag/FA (slag:FA = 40:60) specimen presents the maximum area and an obvious exothermic peak at 861 °C, which is attributed to the decarboxylation of calcite [32], due to the increased C-S-H content between the reactive calcium and silicate.

However, the area of the endothermic peak between 100–200 °C decreases for the 10 wt% SF-containing samples due to the enhanced crosslinking or the propagation of the (N, C)-A-S-H chains, which could combine the Si-OH in Si(OH)₄ monomer and also make the Ca²⁺ involved in C-S-H transform into (N, C)-A-S-H chains as charge balancing

of the negative $\equiv\text{Si-O-Si}\equiv$ chains. Meanwhile, the peak at 861 °C is mainly assigned to the decomposition of calcium carbonate: the slag-rich sample generates some calcium carbonate derived from the reactive CaO with air CO_2 and partial $\text{Ca}(\text{OH})_2$ reacts with the CO_2 at the beginning stage to some extent, especially for the sample (slag:FA = 40:60). However, it disappears for the ternary SF/slag/FA binder. This indirectly indicates that the doped SF facilitates the Ca^{2+} participation in the formation of (N, C)-A-S-H chains, rather than the C-S-H, leading to enhanced freezing–thawing resistance. Generally, the doped SF provides the Si-rich sol system derived from the reactive $\text{Si}(\text{OH})_4$, and the Ca^{2+} in slag is preferred crosslink with $\equiv\text{Si-O-Si}\equiv$ chains transform into he (N, C)-A-S-H chains to from C-S-H, presenting higher freezing–thawing resistance than C-S-H.

3.6. Morphology and Microstructure

The morphological fracture surface of the pastes after 28d curing is presented as a series of electron micrographs with an amplification of 5000 \times in Figure 9a–d. The FA has been partially activated with spherical particles in Figure 9a, displaying the coexistence of the amorphous geopolymer gels. The C-S-H and (N, C)-A-S-H chains are amorphous silicate with irregular shapes, but the C-S-H possesses a shorter chain and angular texture, while the (N, C)-A-S-H chains hold the crosslinking network structure. Partially unreacted spherical FA particles are observed, which gradually disappear with the increasing content of slag, presenting smooth and compact surfaces due to the as-formed C-S-H and (N, C)-A-S-H chain gels as shown in Figure 9c.

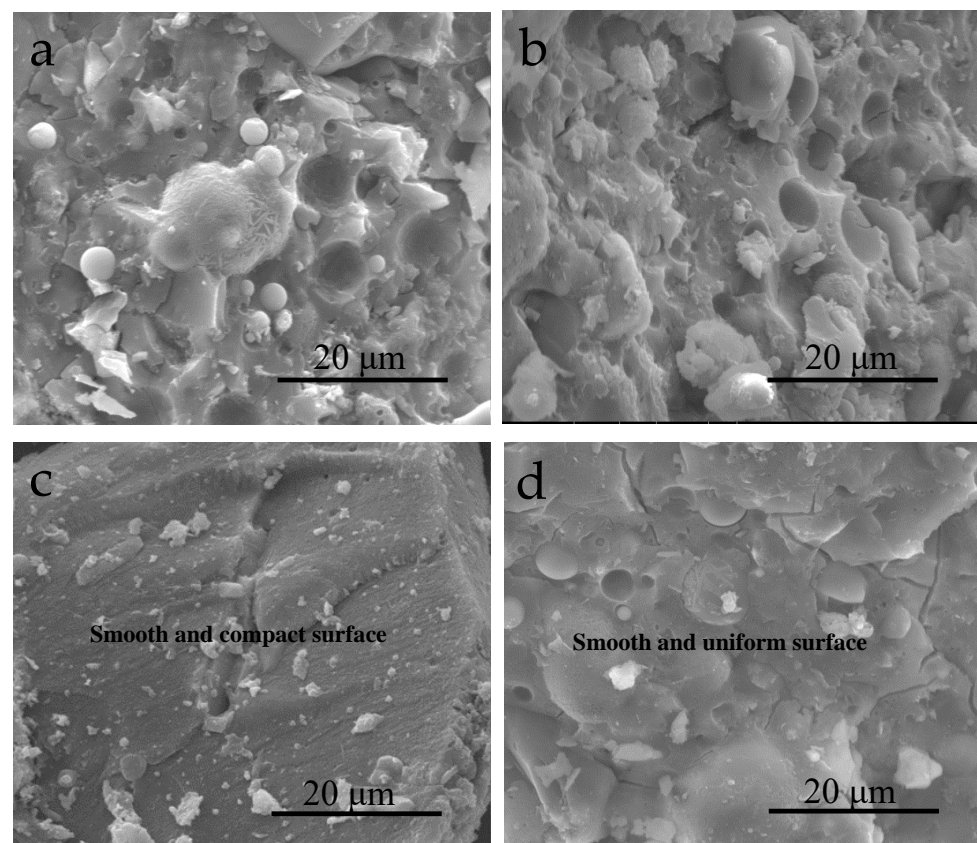


Figure 9. SEM photos of alkali-activated geopolymer paste after 28d-curing at RT (a) incorporating 20 wt% slags into FA, (b) incorporating 30 wt% slags into FA, (c) incorporating 40 wt% slags into FA, (d) incorporating 30 wt% slags and 10 wt% SF into FA.

However, compared with the fracture surface of the SF-containing sample as shown in Figure 9d, the amorphous silicates exhibit a smooth and uniform surface. Spherical FA particles almost disappear, and compact structures are observed, which might be attributed

to the enhanced geopolymerization by doping SF, leading to more network structures. This serves as silicon-aluminate cages for adsorbing Ca^{2+} and $[\text{AlO}_4]^{5-}$, thus inhibiting the C-S-H from growing effectively, corresponding to higher mechanical performance and freezing–thawing resistance. It determines that doped SF plays an important role in microstructure densification by extending the (N, C)-A-S-H chains.

Morphologies of specimens after freeze–thawing cycles are presented as a series of electron micrographs with an amplification of $10,000\times$ in Figure 10a–d. The porous and rugged fracture surface is observed for the specimen without SF after freeze–thawing cycles as shown in Figure 10b,d, compared with the smooth and small-pore fracture in Figure 10a,c. Meanwhile, the ternary SF/slag/FA binder also presents gradual deterioration with increasing freezing–thawing resistance, evidenced by the porous and cracked surface. However, the binary slag/FA binder exhibits even worse deterioration, with the big pores and breakages are shown in Figure 10d.

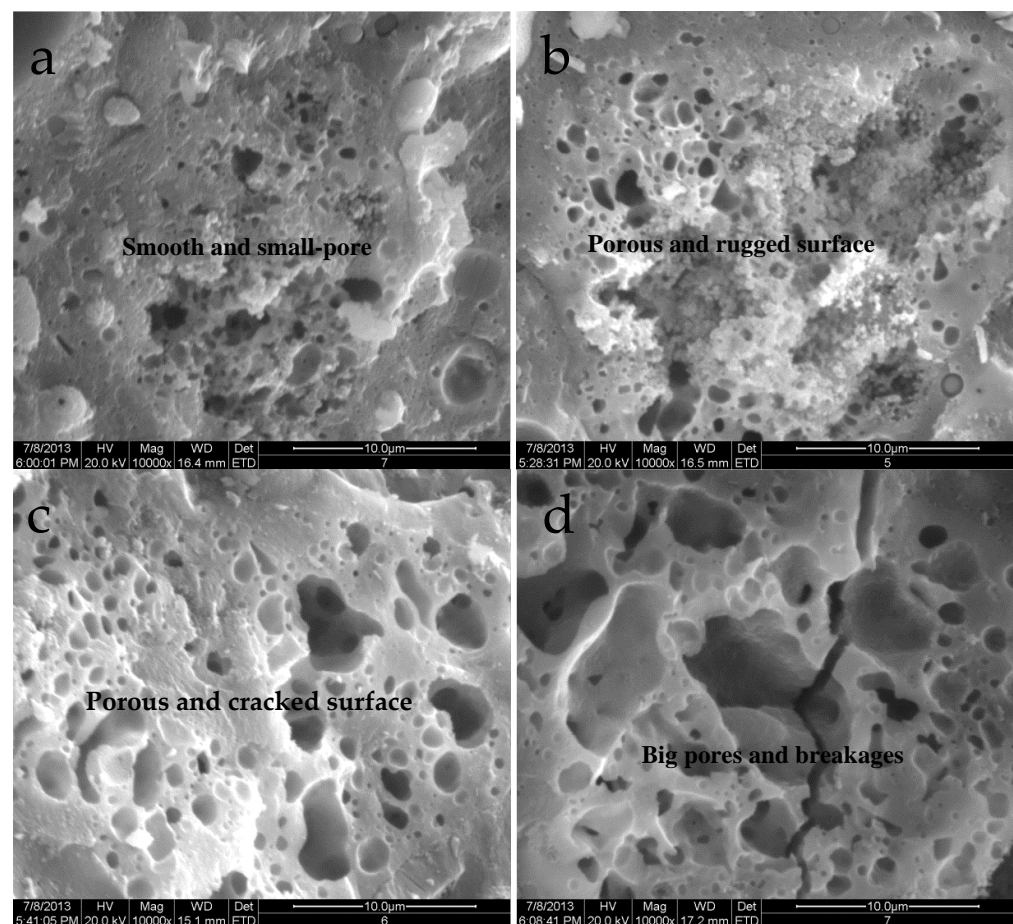


Figure 10. SEM photos of alkali-activated geopolymer paste after freeze–thaw cycles. (a) Incorporating 30 wt% slag and 10 wt% SF into FA after 50 cycles, (b) incorporating 30 wt% slag into FA after 50 cycles, (c) incorporating 30 wt% slag and 10 wt% SF into FA after 125 cycles, (d) incorporating 30 wt% slag into FA after 125 cycles.

This demonstrates that the compact micro-structures of the ternary SF/slag/FA binder inhibit the deterioration during freeze–thawing cycles, combining with the results of MIP. The higher pore volume of larger pores hold a stronger capacity for absorbing free water and favors the greater expansion stress from frost attack, which facilitates the structural damage predominantly. On the other hand, combined with the XRD results, the formation and growth of the amorphous (N, C)-A-S-H gels prompt the compact with higher anti-freezing performance. Behfarnia et al. [33] also assert that nano-SiO₂ particles recover

the particle packing density of the concrete and improve the microstructure as nano-filler, leading to considerable improvement in frost resistance.

Generally, the slag and FA are depolymerized into reactive $[\text{Si}(\text{OH})_4]$ and $[\text{Al}(\text{OH})_4]^-$ under the Na_2SiO_3 activation, the Na_2SiO_3 inherently hydrolyzes into $\equiv\text{Si}-\text{O}-\text{Si}\equiv$ precursor chains which provide the prerequisites of the subsequent chain propagation. The activated calcium involved in slag facilitates the higher mechanical property for heat-free curing. However, there is competition between the formation of C-S-H and amorphous (N, C)-A-S-H silicates (also denoted as $M_n[-(\text{Si}-\text{O}_2)_z-\text{Al}-\text{O}]_n \cdot w\text{H}_2\text{O}$) for the XRD. The latter holds chain structure and favors compact and uniform stacking, while the former is prone to transform disorderly non-uniform microstructure with an increased porosity from the results of SEM and MIP. Meanwhile, incorporating SF provides abundant activated silica tetrahedra $[\text{Si}(\text{OH})_4]$ for the alkali-activated slag/FA system. It promotes the propagation of (N, C)-A-S-H chains through crosslinking between short-chain silicates and $[\text{Si}(\text{OH})_4]$, triggering the formation of cross-linked networks or cages for trapping Ca^{2+} by electrostatic interactions. Because the Ca^{2+} involved in C-S-H is easily attracted and packaged by electrostatic force due to the electronegative $[\text{Al}(\text{OH})_4]^-$, transforming into more (N, C)-A-S-H from incipient C-S-H leads to a decrease in porosity (drops from 19.08% to 13.47%). Thus, it exerts higher mechanical strength during the freezing–thawing cycles, as shown in Figure 11.

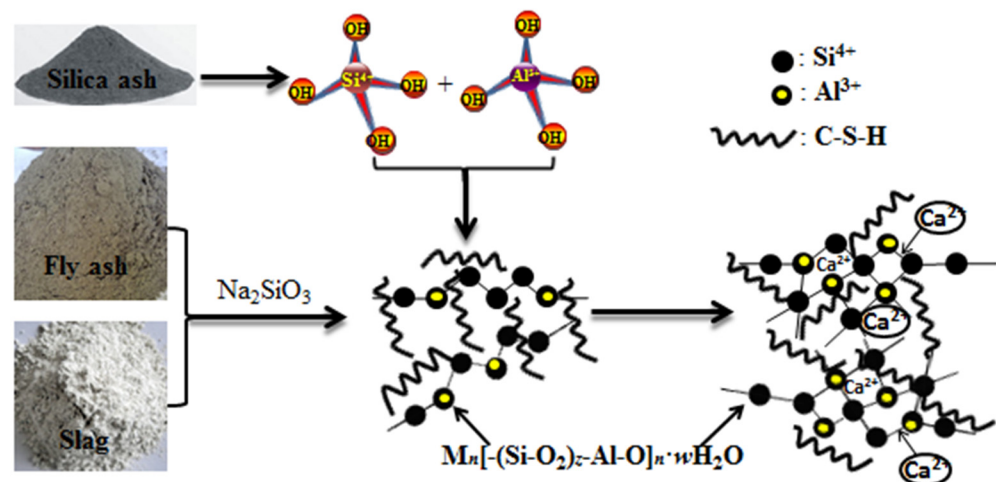


Figure 11. Schematic diagram of the reaction mechanism.

4. Conclusions

A simple-yet-effective solution for the utilization of industrial solid wastes is explored in this paper, and the optimum slag dosage in heat-free curing alkali-activated slag/FA-based geopolymer is determined. Meanwhile, the SF is employed to construct the ternary slag/FA/SF (SF:slag:FA = 10:30:60, wt%) paste through the replacement of FA with 10 wt% SF and the following conclusions are drawn.

(1) An appropriate dosage (30 wt%) of slag is necessary to attain heat-free alkali-activated slag/FA geopolymer paste with excellent mechanical strength. The incorporated 10 wt% SF as starting material is an effective approach to further alleviate its inherent fragility, evidenced by the compressive and flexural strength of 95.2 and 3.2 MPa, respectively.

(2) Incorporation of 10 wt% SF promotes the propagation of (N, C)-A-S-H chains rather than the formation of C-S-H. It is evidenced by the absent exothermic peak at about 861 °C from the DSC curves, leading to the increases in the pores volume with a pore diameter < 20 nm and tortuosity by MIP results.

(3) The ternary slag/FA/SF paste exerts an improved freezing–thawing resistance with a residual compressive strength of 52.8 MPa and a weight loss of 10.5% after 300 freeze–thawing cycles.

Author Contributions: Conceptualization, Y.W. and S.W.; methodology, Y.L.; software, D.M.; validation, C.Z., J.X. and X.S.; formal analysis, Y.W.; investigation, S.W.; resources, S.W.; data curation, Y.L.; writing—original draft preparation, D.M.; writing—review and editing, Y.W.; visualization, S.W.; supervision, Y.W.; project administration, S.W.; funding acquisition, S.W. All authors have read and agreed to the published version of the manuscript.

Funding: The project is supported by the Natural Science Foundation of Shaanxi Province (2021CGBX-36).

Data Availability Statement: Not applicable.

Conflicts of Interest: The authors declare no conflict of interest.

References

1. Wang, S.; Liu, B.; Zhang, Q.; Wen, Q.; Lu, X.; Xiao, K.; Ekberg, C.; Zhang, S. Application of geopolymers for treatment of industrial solid waste containing heavy metals: State-of-the-art review. *J. Clean. Prod.* **2023**, *390*, 136053. [[CrossRef](#)]
2. He, M.; Yang, Z.; Li, N.; Zhu, X.; Fu, B.; Ou, Z. Strength, microstructure, CO₂ emission and economic analyses of low concentration phosphoric acid-activated fly ash geopolymer. *Constr. Build. Mater.* **2023**, *374*, 130920. [[CrossRef](#)]
3. Peng, X.; Li, H.; Hu, Y. Preparation of metakaolin-fly ash cenosphere based geopolymer matrices for passive fire protection. *J. Mater. Res. Technol.* **2023**, *23*, 604–610. [[CrossRef](#)]
4. Raut, A.; Murmu, A.; Alomayri, T. Physico-Mechanical and thermal behavior of prolong heat Cured geopolymer blocks. *Constr. Build. Mater.* **2023**, *370*, 130309. [[CrossRef](#)]
5. Harmal, A.; Khouchani, O.; El-Korchi, T.; Tao, M.; Walker, H.W. Bioinspired brick-and-mortar geopolymer composites with ultra-high toughness. *Cem. Concr. Compos.* **2023**, *137*, 104944. [[CrossRef](#)]
6. Oh, J.; Monteiro, P.; Jun, S.; Choi, S.; Clark, S.M. The evolution of strength and crystalline phases for alkali-activated ground blast furnace slag and fly ash-based geopolymers. *Cem. Concr. Res.* **2010**, *40*, 189–196. [[CrossRef](#)]
7. Chithiraputhiran, S.; Neithalathm, N. Isothermal reaction kinetics and temperature dependence of alkali activation of slag, fly ash and their blends. *Constr. Build. Mater.* **2013**, *45*, 233–242. [[CrossRef](#)]
8. Ismail, I.; Bernal, S.; Provis, J.; Hamdan, S.; van Deventer, J.S. Microstructural changes in alkali activated fly ash/slag geopolymers with sulfate exposure. *Mater. Struct.* **2013**, *46*, 361–373. [[CrossRef](#)]
9. Chi, M.; Huang, R. Binding mechanism and properties of alkali-activated fly ash/slag mortars. *Constr. Build. Mater.* **2013**, *40*, 291–298. [[CrossRef](#)]
10. Zhang, Y.; Wang, Y.; Xu, D.L.; Li, S. Mechanical performance and hydration mechanism of geopolymer composite reinforced by resin. *Mat. Sci. Eng. A Struct.* **2010**, *527*, 6574–6580. [[CrossRef](#)]
11. Zhang, Y.; Li, S.; Wang, Y. Microstructural and strength evolutions of geopolymer composite reinforced by resin exposed to elevated temperature. *J. Non Cryst. Solid* **2012**, *358*, 620–624. [[CrossRef](#)]
12. Yan, S.; Pan, D.; Dan, J.; Wang, J.; Yu, Y. Calcium carbide residue and Glauber’s salt as composite activators for fly ash-based geopolymer. *Cem. Concr. Compos.* **2023**, *140*, 105081. [[CrossRef](#)]
13. Yang, J.; Bai, H.; He, X.; Zeng, J.; Su, Y.; Wang, X.; Zhao, H.; Mao, C. Performances and microstructure of one-part fly ash geopolymer activated by calcium carbide slag and sodium metasilicate powder. *Constr. Build. Mater.* **2023**, *367*, 130303. [[CrossRef](#)]
14. Wang, H.; Zhao, X.; Gao, H.; Yuan, T.; Zhang, X. The effects of salt-loss soda residue and oxalate acid on property and structure of fly ash-based geopolymer. *Constr. Build. Mater.* **2023**, *366*, 130214. [[CrossRef](#)]
15. El-Mir, A.; Hwalla, J.; El-Hassan, H.; Assaad, J.J.; El-Dieb, A.; Shehab, E. Valorization of waste perlite powder in geopolymer composites. *Constr. Build. Mater.* **2023**, *368*, 130491. [[CrossRef](#)]
16. Susan, A.; Bernal, E.D.; Rodriguez, R.M.d.G.; John, L.P.; Silvio, D. Activation of metakaolin/slag blends using alkaline solutions based on chemically modified silica fume and rice husk ash. *Waste Biomass Valor* **2012**, *3*, 99–108.
17. Garcia, J.I.; Villanueva, V.M.; Gorokhovskiy, A.V.; Mendoza-Suárez, G.; Fuentes, A.F. Characteristics of a NaOH-activated blast furnace slag blended with a fine particle silica waste. *J. Am. Ceram. Soc.* **2002**, *85*, 1788–1792. [[CrossRef](#)]
18. Maheepala, M.; Nasvim, M.; Robert, D.; Gunasekara, C.; Kurukulasuriya, L.C. A comprehensive review on geotechnical properties of alkali activated binder treated expansive soil. *J. Clean. Prod.* **2022**, *363*, 132488. [[CrossRef](#)]
19. Zhang, H.; Kumar, S.P.; Xiao, L.; Ai, J.; He, B.; Ren, Q.; Zhu, X.; Zhang, Y. Durability of low-carbon geopolymer mortar: Different responses to cryogenic attack caused by water content and freeze-thaw mediums. *Cem. Concr. Compos.* **2023**, *139*, 105065. [[CrossRef](#)]
20. Jiao, Z.; Li, X.; Yu, Q. Effect of curing conditions on freeze-thaw resistance of geopolymer mortars containing various calcium resources. *Constr. Build. Mater.* **2021**, *313*, 125507. [[CrossRef](#)]
21. Mardani-Aghabaglou, A.; Sezer, G.I.; Ramyar, K. Comparison of fly ash, silica fume and metakaolin from mechanical properties and durability performance of mortar mixtures view point. *Constr. Build. Mater.* **2014**, *70*, 17–25. [[CrossRef](#)]
22. Puligill, S.; Mondal, P. Role of slag in microstructural development and hardening of fly ash-slag geopolymer. *Cem. Concr. Res.* **2013**, *43*, 70–80. [[CrossRef](#)]
23. Provis, J.; Myers, R.; White, C.; Rose, V.; Van Deventer, J.S. X-ray microtomography shows pore structure and tortuosity in alkali-activated binders. *Cem. Concr. Res.* **2012**, *42*, 855–864. [[CrossRef](#)]

24. Song, S.; Sohn, D.H.M.; Jennings, T.; Mason, O. Hydration of alkali-activated ground granulated blast furnace slag. *J. Mater. Sci.* **2000**, *35*, 249–257. [[CrossRef](#)]
25. Collins, F.; Sanjayan, J. Unsaturated Capillary Flow within alkali activated slag concrete. *J. Mater. Civ. Eng.* **2008**, *20*, 565–570. [[CrossRef](#)]
26. Ma, H.; Yu, H.; Sun, W. Freezing–thawing durability and its improvement of high strength shrinkage compensation concrete with high volume mineral admixtures. *Constr. Build. Mater.* **2013**, *39*, 124–128. [[CrossRef](#)]
27. Garbalinska, H.; Wygocka, A. Microstructure modification of cement mortars: Effect on capillarity and frost-resistance. *Constr. Build. Mater.* **2014**, *51*, 258–266. [[CrossRef](#)]
28. Sun, P.; Wu, H. Chemical and freeze–thaw resistance of fly ash-based inorganic mortars. *Fuel* **2013**, *111*, 740–745. [[CrossRef](#)]
29. Abadel, A.; Alghamdi, H. Effect of high volume tile ceramic wastes on resistance of geopolymers mortars to abrasion and freezing–thawing cycles: Experimental and deep learning modelling. *Ceram. Int.* **2023**, *49*, 15065–15081. [[CrossRef](#)]
30. Li, F.; Chen, D.; Lu, Y.; Zhang, H.; Li, S. Influence of mixed fibers on fly ash based geopolymer resistance against freeze–thaw cycles. *J. Non Cryst. Solids* **2022**, *584*, 121517. [[CrossRef](#)]
31. Chen, C.; Lu, C.; Lu, C.; Wei, S.; Guo, Z.; Zhou, Q.; Wang, W. Synergetic effect of fly ash and ground-granulated blast slag on improving the chloride permeability and freeze–thaw resistance of recycled aggregate concrete. *Constr. Build. Mater.* **2023**, *365*, 130015. [[CrossRef](#)]
32. Rashad, A.M. An investigation on very high volume slag pastes subjected to elevated temperatures. *Constr. Build. Mater.* **2015**, *74*, 249–258. [[CrossRef](#)]
33. Behfarnia, K.; Salemi, N. The effects of nano-silica and nano-alumina on frost resistance of normal concrete. *Constr. Build. Mater.* **2013**, *48*, 580–584. [[CrossRef](#)]

Disclaimer/Publisher’s Note: The statements, opinions and data contained in all publications are solely those of the individual author(s) and contributor(s) and not of MDPI and/or the editor(s). MDPI and/or the editor(s) disclaim responsibility for any injury to people or property resulting from any ideas, methods, instructions or products referred to in the content.